ADVANCED FUNCTIONAL MATERIALS
www.afm-journal.de

Check for updates

# Reconfiguration, Camouflage, and Color-Shifting for Bioinspired Adaptive Hydrogel-Based Millirobots

*Xuemin Du,* Huanqing Cui, Tiantian Xu, Chenyang Huang, Yunlong Wang, Qilong Zhao, Yangsheng Xu, and Xinyu Wu**

**Nature provides much inspiration for developing soft millirobots. However, compared with smart and adaptations of lives in nature, these robotic systems still suffer from insufficiency of intelligence. Here, a new untethered soft millirobot with magnetic actuation in the head and function in the tail is presented via implementing control, actuation, and sensing directly in the materials, thereby endowing robots with multimodal locomotion and environment-adaptive functions. Due to the soft and asymmetric structure, the millirobot not only shows robust multimodal locomotion, including controllable and transformable crawling, swinging and rolling, but also achieves an excellent capability of helical propulsion in water. Moreover, the robot also possesses outstanding obstacle-crossing abilities, including helically propelling over obstacles (>2 body length), crawling within a 2 mm height tunnel and swinging through a 450 µm width channel. Furthermore, the robot can even squeeze its body to crawl through a tube easily via near-infrared irradiation, which triggers the osmotic shrinking of its body. Notably, the robots also possess extraordinary environment-adaptive functions, for example, leptocephali-like optical camouflage in water, octopus-like controllable delivery and variable appearance via visible color–shifting for interaction with the changing environment. These smart robotic systems would be of benefit in various fields via seamless integration of bioinspired design and smart materials.**

## 1. Introduction

In order to better adapt to the complex and ever-changing environment, many marine organisms have evolved with distinctive capabilities. For example, not only do octopuses with soft structures possess diverse locomotion modes, including crawling and swimming, but they can also squeeze into very narrow spaces or produce ultra-fast changes in appearance for escape and disguise.[1,2] Other sea animals such as leptocephali (transparent larvae of eels) have remarkable abilities of agile motions (e.g., swinging) and optical camouflage in water, because their tissues and organs are mainly composed of active transparent hydrogels.[3] All these outstanding adaptations result from their soft structures and smart properties (e.g., robust actuations and adaptive functions) enabling these marine organisms to effectively capture preys and escape from predators.

Inspired by these intelligent adaptations in nature, many efforts have been made on the exploration of various untethered small-scale (from several centimeters down to nanometers in all dimensions) robots that can be driven by chemical fuels,[4–9] light,[10–12] acoustic radiation force,[13] electrical and magnetic fields,[14–20] etc. These actuation mechanisms have been employed to design various small-sized, high-speed, and motion-controllable robots for environmental and biomedical applications.[21–29] Among these systems, magnetic actuation is more practical to various applications not only due to its remotely controllable actuating fields, but also due to its facile and harmless penetration into most biological and artificial materials.[24,25,30–32] Conventionally, magnetic small-scale robots were fabricated with rigid materials, which usually have no more than five actuated degrees of freedom under a magnetic field. Recently, soft robots were prepared with elastomers or responsive polymers, which have greater potential to realize high mobility via multimodal locomotion, because such bioinspired systems have higher degrees of freedom than those with rigid structures.[33] In a seminal work, Hu et al. developed soft-bodied millirobots via embedding hard magnetic microparticles into an entire non-responsive silicone elastomer body, which shall show multimodal locomotion due to the symmetric shape change of the flexible body.[34] However, these systems not only lack the abilities of programmable behaviors owing to the non-responsive properties of silicone elastomer, but also struggle with errors in locomotion resulting from non-uniform deformations of the body due to the residual strain energy from the fabrication process. Recently, various programmed robots

Prof. X. Du, H. Cui, Dr. Y. Wang, Dr. Q. Zhao
Institute of Biomedical and Health Engineering
Shenzhen Institutes of Advanced Technology (SIAT)
Chinese Academy of Sciences (CAS)
Shenzhen 518035, China
E-mail: xm.du@siat.ac.cn

Dr. T. Xu, C. Huang, Prof. X. Wu
Guangdong Provincial Key Laboratory of Robotics and Intelligent System
Shenzhen Institutes of Advanced Technology (SIAT)
Chinese Academy of Sciences (CAS)
Shenzhen 518035, China
E-mail: xy.wu@siat.ac.cn

Prof. Y. Xu
Robotics and Artificial Intelligence Laboratory
The Chinese University of Hong Kong, Shenzhen
Shenzhen Institute of Artificial Intelligence and Robotics for Society
Shenzhen 518172, China

The ORCID identification number(s) for the author(s) of this article can be found under https://doi.org/10.1002/adfm.201909202.

**DOI: 10.1002/adfm.201909202**

 © 2020 WILEY-VCH Verlag GmbH & Co. KGaA, Weinheim

have been further developed by patterning magnetic particles in responsive polymer composites. These robots possess excellent programmable 3D swimming capabilities but no adaptive functions.[35,36] These soft materials may have paved important ways for controllable motions, but compared with the smart adaptations in nature, the overall robotic systems still suffer from insufficiency of intelligence. The process to implement control, actuation, and sensing (e.g., robust motion, reconfiguration, camouflage, and interaction with the changing environment) directly in the materials, thereby enabling soft robots with smart behaviors, is intriguing yet challenging.

Here, by mimicking the smart features in nature, we present a new untethered soft millimeter-scale robot with a magnetic head and a non-magnetic tail (length of the head: ≈1 mm, length of the tail: 5 mm, width: ≈1 or 4 mm, height: ≈174 μm) made of reversibly temperature-responsive hydrogel (poly(*N*-isopropylacrylamide), PNIPAM) embedded with neodymium-iron-boron (NdFeB) microparticles to overcome the existing challenges inherent in conventional soft robots. This intelligent robot—the iRobot—not only shows robust multimodal locomotion, including controllable and transformable crawling, swinging, and rolling in water, but also achieves an excellent capability of helical propulsion in water due to the soft and well-designed asymmetric structure, where NdFeB particles were solely in the head of the hydrogel robot. Moreover, the robot also demonstrates outstanding obstacle-crossing abilities, for example, helically propelling over obstacles (across obstacle >2 body length), crawling within a low tunnel (height: ≈2 mm), and swinging through a narrow channel (width: ≈450 μm). Furthermore, the iRobot can even squeeze its body (≈35% of its own size) to go through a narrow tube easily under near-infrared (NIR, 808 nm) irradiation that triggers the osmotic shrinking of PNIPAM hydrogel embedded with gold nanorods (AuNRs). Notably, the iRobot also possesses extraordinary functions, for example, optical camouflage in water, controllable delivery, and interaction with the changing environment via visible color–shifting. To the best of our knowledge, this is the first hydrogel robot that not only demonstrates robust multimodal locomotion, but also possesses unprecedented environment-adaptive functions of configuration, camouflage, and color-shifting dependent on the unique structural design and responsive properties of hydrogel. This shows that our newly developed soft robots composed of intelligent materials can overcome the existing limitations and exhibit superior functionalities, providing greater possibilities for soft robots to achieve smarter adaptation in various fields.

## 2. Results and Discussion

### 2.1. Design of the Hydrogel-Based Millirobots

Typically, the hydrogel-based millirobots were fabricated by two-step photopolymerization. As shown in **Figure 1**A, NdFeB microparticles were added into a NIPAM prepolymer solution, and then dispersed sufficiently with ultrasound. The prepolymer was added into a tailor-made device of a polymer spacer (1 mm × 5 cm, 200 μm thick) sandwiched by two glass slides, and subsequent UV-induced (365 nm) polymerization to form a NdFeB microparticles-embedded PNIPAM film (the head of the millirobot). After the residual solution was removed and a larger polymer spacer (6 mm × 5 cm, 200 μm thick) was used, only a PNIPAM precursor solution was added into the spacer with the preformed NdFeB microparticles-embedded PNIPAM hydrogel, followed by the second photopolymerization. Afterward, the hydrogel film was peeled off and washed with amount of water to remove the residues.

The hydrogel films were then exposed to a very strong and spatially uniform external permanent magnetic field (≈700 mT) from a tailor-made setup (Figure S1, Supporting Information). After magnetization, the orientation of the magnetic polarization of the hydrogel films is horizontally aligned, which is determined by the external magnetic field. Finally, the hydrogel-based millirobots with NdFeB particles solely in the head (actuation from the 1 mm length head and function from the 5 mm length tail) were facilely obtained in large quantity via cutting the hydrogel film with certain widths and lengths (174 μm thick). Different from ferrite materials, NdFeB microparticles have high remanent magnetization and larger magnetic coercivity, which ensure that the magnetization profile (M) can be maintained during magnetic actuation, thus enabling excellent magnetic actuation of robots.[37–39] Moreover, this unique design of magnetization profile solely within the head of iRobot enables greater potential not only to realize high mobility, but also to achieve outstanding functions.

### 2.2. Multimodal Locomotion of the iRobot

After the magnetization profile **M** is programmed, the iRobot (the Young's modulus of the PNIPAM is ≈37.2 kPa; Figure S2, Supporting Information) can be actuated by an external magnetic field (**B**) to generate various modes of shape deformations. To clearly describe the effects of **B** on the actuations, we express $\mathbf{B} = [B_x, B_y, B_z]^T$ with respect to the robot's head frame, where $\mathbf{B}_{xy}$ represents the *x*–*y* plane components, and $\mathbf{B}_{xz}$ represents the *x*–*z* plane components of B, that is $\mathbf{B}_{xy} = [B_x, B_y]^T$ and $\mathbf{B}_{xz} = [B_x, B_z]^T$. The interaction between **B** and **M** produces spatially changing magnetic torques that induce the deformations of the iRobots, because the magnetization profile **M** of a robot always tends to align with **B**. As shown in **Figure 2**, the robot can change its shape from initial planar film into asymmetric curving, waving, rolling, and helical structures via applying a vertical oscillating magnetic field at *x*–*z* plane, a horizontal oscillating magnetic field at *x*–*y* plane, a rotating magnetic field at *x*–*z* plane, and a conical magnetic field with a constant magnetic field along the *z* axis, respectively (Section S2, Figure S3, Supporting Information). As the external magnetic field is removed, the asymmetrically deformed robot recovers to its initial flat structure, and the flat-deformed structure can be switched repeatedly. These asymmetrical deformations result from the deformation hysteresis of the iRobot tail, which is induced by a varying torque from the head of the iRobot due to the magnetization profile solely within the head (Figure S4, Supporting Information). Notably, the spatially uniform magnetic field and the perfectly flat shape (indicating that no residual strain energy exists during the preparation process) together with the asymmetrical deformation of the iRobot ensure precise control and robust actuation.[34]


© 2020 WILEY-VCH Verlag GmbH & Co. KGaA, Weinheim

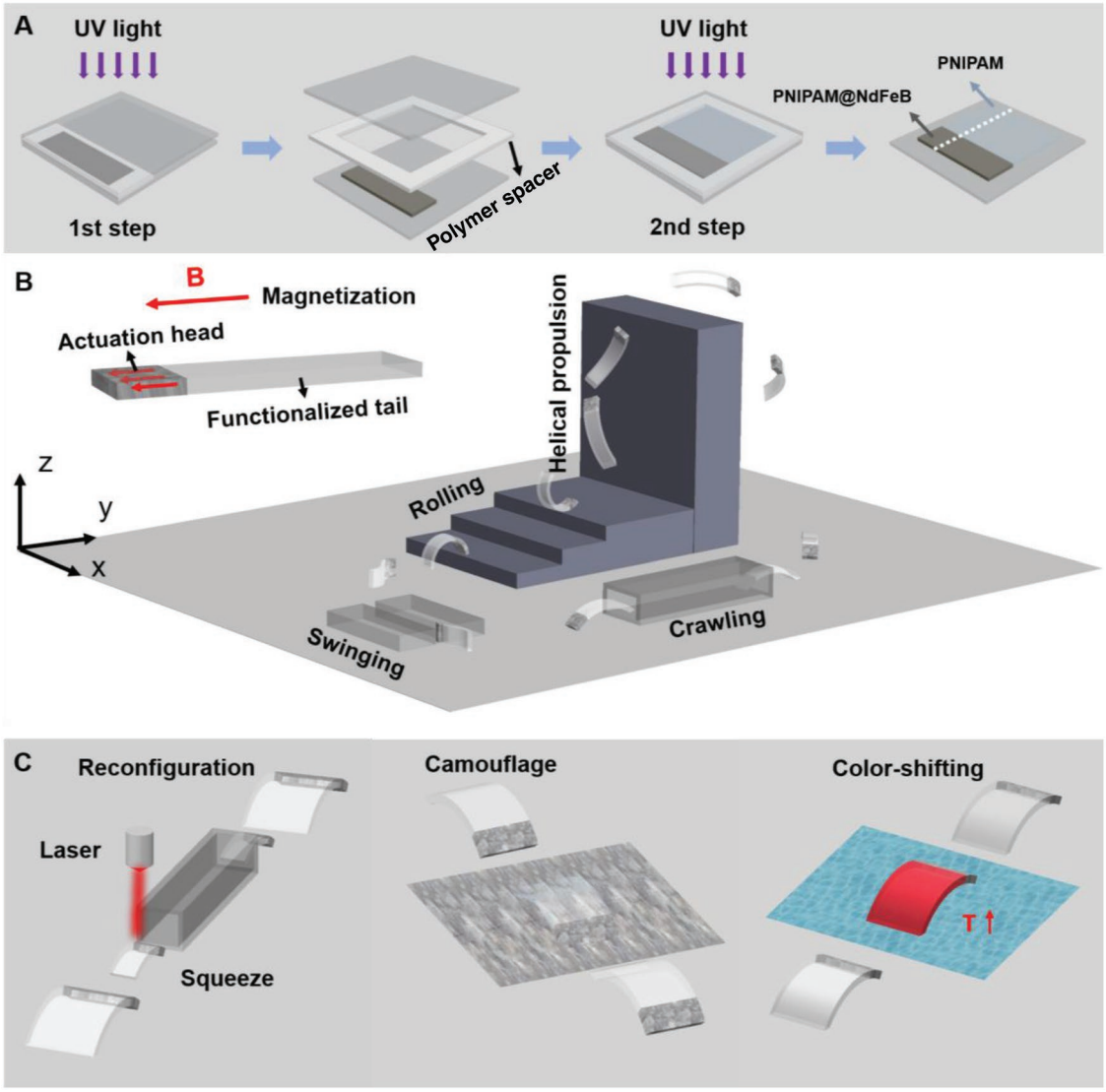


**Figure 1.** Schematic illustration of the design and performances of the hydrogel-based millirobots (iRobot). A) Schematic illustration of the two-step photopolymerization of the hydrogel films. B) Schematic illustration of the magnetization and multimodal locomotion (e.g., crawling, swinging, rolling and helical propulsion) of the iRobot. C) Schematic illustration of the adaptive functions, such as reconfiguration, camouflage, and color-shifting of the iRobot.

Depending on the magnetic actuation mechanism, multimodal locomotion including crawling, swinging, rolling, and helical propulsion can be achieved in water with a Reynolds number ranging from 21 to 36 via applying a time-varying magnetic field. As shown in Figure 2A, the iRobot can crawl straight and fast under exposure to a vertical oscillating magnetic field (≈10 mT) with a frequency of 2.6 Hz at *x*–*z* plane ($\mathbf{B}_{xz}$), resulting in relative vertical displacement due to the periodical time-varying shapes at *x*–*z* plane (Movie S1, Supporting Information). While applying a horizontal oscillating magnetic field (≈10 mT) with a frequency of 3.6 Hz at *x*–*y* plane ($\mathbf{B}_{xy}$), the iRobot can demonstrate leptocephali-like behaviors (Figure 2B; Movie S2, Supporting Information). Because the robot's deformations are small in these two demonstrations, a traveling wave can be created along the robot's body by using an oscillating magnetic field, thus producing effective motions. Interestingly, the iRobot can also roll fast via applying a rotating magnetic field. As shown in Figure 2C (Movie S3, Supporting Information), the iRobot changes its shape from planar structure into asymmetric C shape and fast rolls forward as applying a *x*–*z*-plane magnetic field ($\mathbf{B}_{xz}$, ≈10 mT). As the robot's $\mathbf{M}$ is always parallel to the applied $\mathbf{B}_{xz}$ in small-deflection conditions, the robot's tail switches between the storage and release of the elastic potential energy in a rotation cycle. Unlike a rigid rolling body, the elastic rolling tail has the potential for mobility over a wide range of terrain types at high speeds, such as a steep slope and stairs. Impressively, when applying a conical magnetic field, the iRobot even can helically propel in water (Figure 2D; Movie S4, Supporting Information), which is an excellent achievement for soft robots. These outstanding locomotion modes of the iRobot resulted from the uniform B, perfectly flat hydrogel film, and asymmetric structure, ensuring


© 2020 WILEY-VCH Verlag GmbH & Co. KGaA, Weinheim

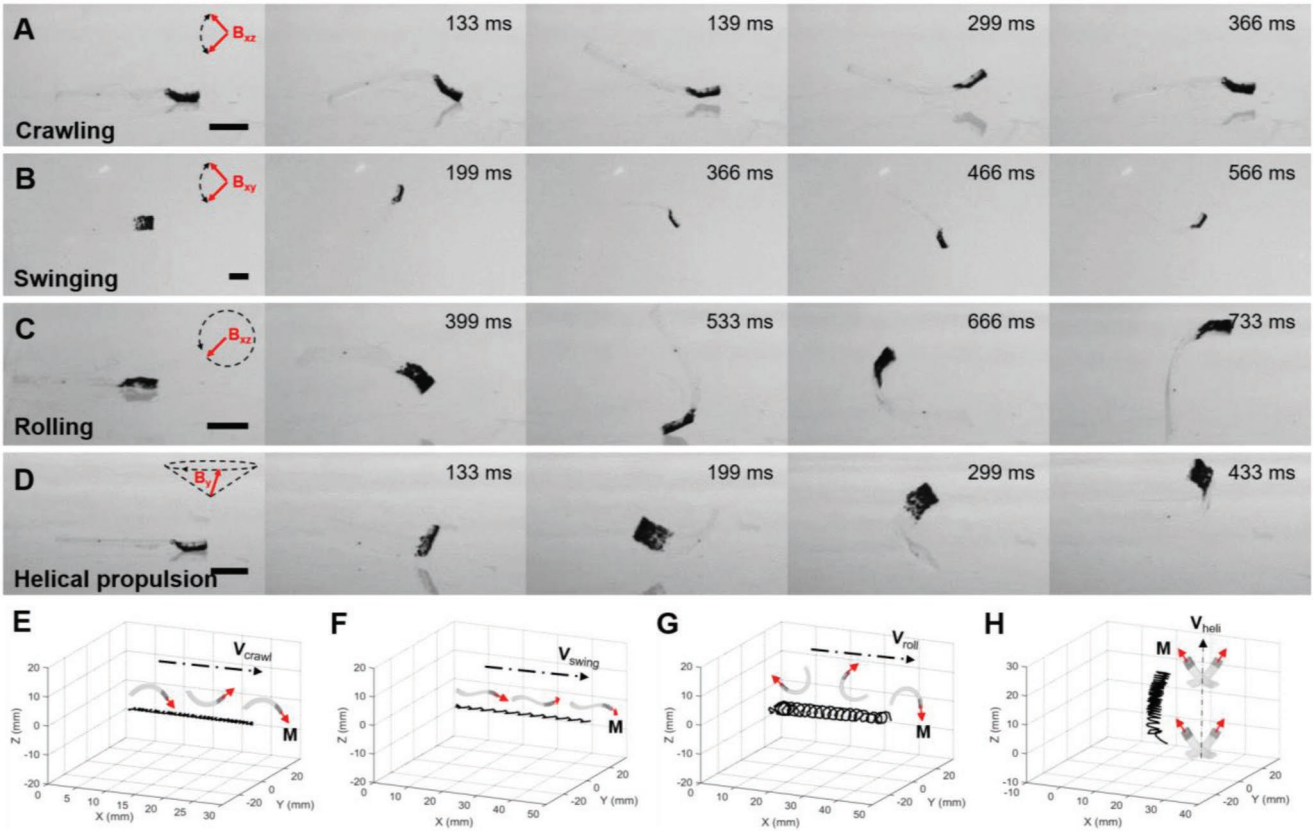


**Figure 2.** Locomotion performances. A) The iRobot crawls (side view) in water at room temperature under exposure to a vertical oscillating magnetic field (≈10 mT) with a frequency of 2.6 Hz at *x*–*z* plane. The corresponding video is shown in Movie S1, Supporting Information. B)The iRobot swings (top view) in water at room temperature under exposure to a horizontal oscillating magnetic field (≈10 mT) with a frequency of 3.6 Hz at *x*–*y* plane. The corresponding video is shown in Movie S2, Supporting Information. C) The iRobot rolls (side view) in water at room temperature under exposure to a rotating magnetic field (≈10 mT) with a frequency of 2.6 Hz at *x*–*y* plane. The corresponding video is shown in Movie S3, Supporting Information. D) The iRobot helically propels (side view) in water at room temperature under exposure to a conical magnetic field (≈10 mT) with a frequency of 6.1 Hz. The corresponding video is shown in Movie S4, Supporting Information. E–H) Visualizing the workspaces of the same robot as crawling, swinging, rolling, and helical propulsion from side view, top view, side view, and side view, respectively. The scale bars are 1 mm.

continuous linear trajectory in various locomotion modes with a very low magnetic field and frequency (Figure 2E–H).

To further validate various locomotion, we compared these experimental characterizations against extensive theoretical models conducted across hydrogel robots with different designs. Generally, the models are in good agreement with our experimental data (see Section S3, Figure S4–S18, Supporting Information). Detailed discussions on the experimental and theoretical correspondence of crawling, swinging, rolling, and helical propulsion can be found in Section S3, Supporting Information. It is worth noting that these analyses could also provide useful design rules for optimizing the performances of future soft robots that obtain various locomotion (see Section S3, Figure S18 and S19, Movie S5, Supporting Information).

In nature, many organisms always use diverse locomotion modes to escape from their predators, like octopus. Our iRobot can also achieve series of locomotion modes to move through complex liquid–solid environment (Movie S6, Supporting Information). As shown in **Figure 3**A, the iRobot first rolls across the stairs (height: ≈1 mm, linear distance: ≈2.8 cm) in 7 s. Subsequently, the iRobot demonstrates excellent obstacle-crossing ability, which swims over a standing obstacle with a height of 1.3 cm (>2 body length) in 14 s. To speed up, the iRobot quickly crawls away in 4 s after landing. Under the fast-alternative orientation of the external magnetic field, the same iRobot can demonstrate series of locomotion modes (Figure 3B), which enables extraordinary task-performing capabilities.

### 2.3. Multifunction of the iRobot

In addition to robust locomotion capabilities, many organisms also possess unique and outstanding functions.[33] For example, octopus not only can move through a tiny space, squeeze its body into a narrow space, but also hide itself via camouflage.[1] By mimicking the excellent functions of natural organisms, we further verify the performances of the iRobot in several harsh environments, including a low tunnel with a height of 2 mm, a narrow channel with a width of 450 µm, and a cubic tube with an inner width of 3 mm (**Figure 4**). Previously, it has been recognized that moving through a tiny space (similar to the size of millirobot) is very challenging due to the difficulty of precision manipulation. In our work, the perfectly flat and soft structure of our robot together with the uniform


© 2020 WILEY-VCH Verlag GmbH & Co. KGaA, Weinheim

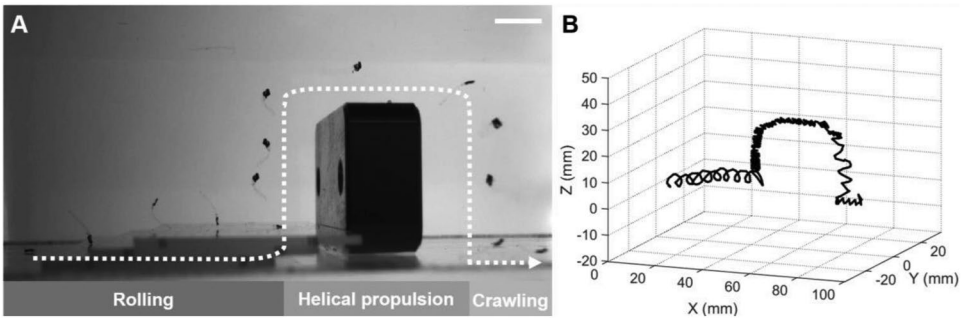


**Figure 3.** Multimodal locomotion for crossing obstacles. A) The iRobot rolls to step stairs (linear distance: 2.8 cm), helically propels over a standing obstacle (height: ≈1.3 cm), finally lands and crawls away in water at room temperature. The corresponding video is shown in Movie S6, Supporting Information. B) Visualizing the workspaces of this multimodal locomotion. The scale bar is 5 mm.

magnetic field ensures the precise locomotion. As a result, the iRobot can easily crawl through the 2 mm height tunnel with an average speed of 0.83 mm $s^{-1}$ underwater (Figure 4A,B; first part of Movie S7, Supporting Information). In addition, the iRobot can still swing through a 450 µm wide channel with an average speed of 0.18 mm $s^{-1}$ underwater, which is only 2.5-folds of its own thickness (Figure 4C,D; second part of Movie S7, Supporting Information). Moreover, the iRobot even can shrink itself to crawl through a cubic tube, where the inner width (≈3 mm) of the tube is smaller than the width of the robot (length: ≈6 mm, width: ≈4.0 mm, height: ≈174 µm) (Figure 4E–H; Movie S8, Supporting Information). This outstanding property results from the unique thermal-responsive properties of PNIPAM, which has a low critical solution temperature (LCST) at ≈32 °C. Thus, the hydrogel shrinks upon heating above LCST due to the transition from a hydrated to a dehydrated phase. On the contrary, the hydrogel swells in the environment temperature below LCST. As shown in

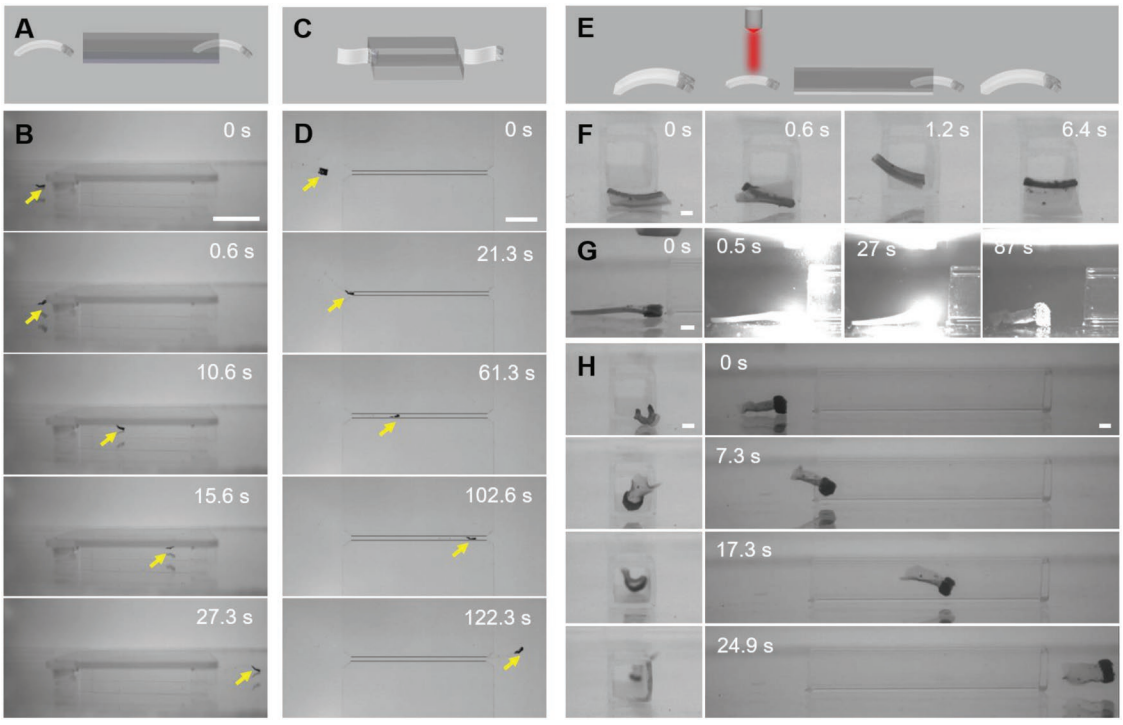


**Figure 4.** Reconfiguration function. A) Schematic illustration of an iRobot going through a low tunnel. B) The iRobot crawls through a 2 mm height tunnel with an average speed of 0.83 mm $s^{-1}$ underwater at room temperature. The corresponding video is shown in Movie S7, Supporting Information. C) Schematic illustration of an iRobot navigating through a narrow channel. D) The iRobot swings through a 450 µm wide channel with an average speed of 0.18 mm $s^{-1}$ underwater at room temperature. The corresponding video is shown in second part of Movie S7, Supporting Information. E) Schematic illustration of an iRobot squeezing through a cubic tube with a smaller size than its own under exposure to NIR irradiation. F) The iRobot cannot crawl forward due to its larger size (length: ≈6 mm, width: ≈4.0 mm, height: ≈174 µm) than the tube with an inner width of 3 mm. The corresponding video is shown in Movie S8, Supporting Information. G) As exposure to NIR irradiation at a wavelength 808 nm, the size of the iRobot quickly shrinks to 35% of its own size. The corresponding video is shown in the second part of Movie S8, Supporting Information. H) The squeezed iRobot crawls through the small size tube in 24 s at left side and front side views. The corresponding video is shown in the third part of Movie S8, Supporting Information. The scale bar is 5 mm for panels (C) and (D). The scale bar is 1 mm for panels (F) to (H).


© 2020 WILEY-VCH Verlag GmbH & Co. KGaA, Weinheim

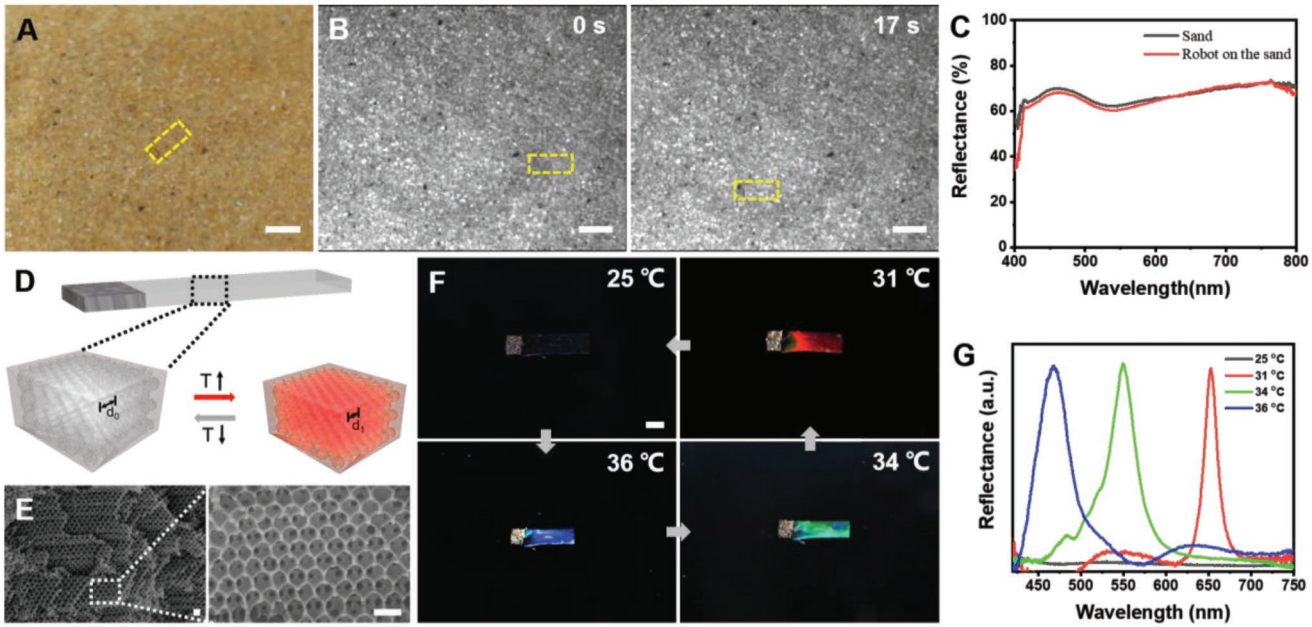


**Figure 5.** Camouflage and color-shifiting of the iRobots. A) Image of a transparent iRobot on the sand. Scale bar: 5 mm. B) The iRobot is hard to be identified on the sand once stopped, and it becomes completely flat by converting its 3D structure to 2D in a fast manner. The corresponding video is shown in Movie S9 and S10, Supporting Information. Scale bar: 5 mm. C) A comparison of the reflectance spectra between the sand and the iRobot on the sand. D) Schematic illustration of a structural-color iRobot, and the mechanism of color change between transparency and red. E) Inverse opal structure of the iRobot and the enlarged scanning electron microscopy (SEM) images. Scale bar: 200 nm. F) The iRobot quickly changes its color from blue to green, red, and transparency as decreasing the temperature from 36 to 34, 31, and 25 °C, respectively. The corresponding video is shown in Movie S11, Supporting Information. G) The Bragg diffraction red shifts as decreasing the temperature from 36 to 34, 31, and 25 °C. Scale bar: 1 mm.

Figure 4F, when the iRobot crawls forward, however, it cannot go through the tube due to its larger size than the tube (first part of Movie S8, Supporting Information). Under exposure to NIR irradiation at a wavelength 808 nm, the size of the iRobot quickly shrinks to 35% of its initial size (Figure 4G; second part of Movie S8, Supporting Information), which is due to the photothermal-responsive properties of PNIPAM hydrogels by coupling embedded AuNRs (Figure S20, Supporting Information). Consequently, the squeezed iRobot can facilely crawl through the tube in 24 s (Figure 4H; third part of Movie S8, Supporting Information), and the iRobot can finally recover to the initial size. Unprecedentedly, this is the first smart soft millirobot that can go through a tiny space that is smaller than its own size. Attributed to the outstanding photothermal-responsive properties of PNIPAM@AuNRs, the iRobot can also show excellent delivery performance under exposure to NIR irradiation, where the loading of rhodamine B is squeezed out due to the large shrinking of the iRobot, thus increasing the absorbance (Figure S21, Supporting Information). These intriguing reconfiguring functions provide much potential for working in harsh environment, for example, in brains, blood vessels, and joints, or even with drug delivery capabilities.

Furthermore, our iRobot can achieve excellent leptocephali-like camouflage in water due to the high transparent property of the hydrogel (**Figure 5**A,B). As shown in Figure 5B, the iRobot is difficult to be identified on the sand once stopped, where the robot can even become completely flat by converting its 3D structure to 2D in a fast manner (Movie S9 and S10, Supporting Information). This transparent soft robot, which contains 90% water, has similar refractive index to water, and thus is capable of minimizing light reflection and refraction and achieving excellent camouflage. Although various soft camouflaging robots have been developed, where the actuation sources are connected via cables,[40–43] few efforts have been made to explore transparent smart soft robots driven remotely by external fields.

Notably, our iRobot can not only achieve excellent configuration and camouflage, but also sense the changing environment via the introduction of structural color into the tail. As shown in Figure S22A, Supporting Information, the precursor was first cast into the voids of the silica colloidal crystals, and then solidified by UV light. Afterward, the iRobot with inverse opal-structured tail was obtained by etching the silica particles and the following the magnetization process (Figure S22, Supporting Information, Figure 5D,E). Due to the feasible thermal property of PNIPAM, the tail of the iRobot is transparent when the environmental temperature is below the LCST. As the temperature increases above LCST (at 36 °C), the iRobot quickly changes its tail color from transparency to blue due to fast osmotic shrinking of PNIPAM, resulting in a blue shift of Bragg diffraction. Interestingly, decreasing the temperature, the iRobot can shift its color from blue to green and even to red (Movie S11, Supporting Information). While the temperature recovers to the initial temperature (T < LCST), the iRobot can recover to its initial transparency due to the reversible osmotic swelling, causing a red shift of Bragg diffraction. The introduction of intelligent materials into the iRobot to achieve highly desirable performance in terms of sensing and responding, therefore, could mean an important step forward in soft robot applications.[33,44–50]


© 2020 WILEY-VCH Verlag GmbH & Co. KGaA, Weinheim

## 3. Conclusion

Inspired by multimodal locomotion and adaptive functions that exist in nature (e.g., octopus, leptocephali), we have designed a hydrogel millirobot, named iRobot, which is not only capable of controllable and reversible multimodal locomotion but also possesses environment-adaptive functions including reconfiguration, camouflage, and sensing the changing environment. Depending on the shape-actuation mechanism, controllable locomotion including crawling, swing, rolling, and helical propulsion can be achieved via applying a time-varying magnetic field. Furthermore, the same iRobot can demonstrate series of transformable locomotion modes via the fast-alternative orientation of the external magnetic field, which enables extraordinary task-performing capabilities. Impressively, the robot also demonstrates outstanding obstacle-crossing abilities, for example, helically propelling over obstacles, crawling within a low tunnel, and swinging through a narrow channel. Furthermore, the iRobot can even squeeze its body to go through a narrow tube (with a smaller size than the robot) easily via NIR irradiation, which triggers the osmotic shrinking of PNIPAM hydrogel embedded with AuNRs. Notably, the iRobots also possess extraordinary functions, for example, leptocephali-like optical camouflage in water, octopus-like controllable delivery, and variable appearance via visible color–shifting for interaction with the changing environment. This seamless integration of bioinspired design and smart materials provides a general and powerful strategy for the development of the next-generation smart robot, which would also inspire the development of smart material systems. Furthermore, these bioinspired smart robots implemented with control, actuation, and sensing directly within the materials would benefit a wide range of fields such as biomedical and environmental fields.

## 4. Experimental Section

*Materials*: *N*-Isopropylacrylamide (NIPAM), *N,N*-methylene-bis-acrylamide (NMBA), cloroauric acid, silver nitrate, sodium borohydride, *N,N*-dimethylformamide (DMF), and rhodamine B were obtained from Sigma-Aldrich. Cetyltrimethyl ammonium bromide (CTAB) was purchased from Sinopharm Chemical Reagent Co., Ltd. 2,2′-Diethoxyacetophenone (DEAP) was obtained from TCI. Hydrofluoric acid (HF) (40%) was purchased from Sinopharm Chemical Reagent. Magnetic neodymium-iron-boron (NdFeB) microparticles with high remanence of 720–760 mT and coercivity of 360–480 A $m^{-1}$ were purchased from Hongyu Technology Co., Ltd. (Figure S4B,C, Supporting Information). All reagents were used as received. Ultra-pure water was used in all the experiments.

*Fabrication of the Hydrogel-Based Millirobots*: Hydrogel-based millirobots based on PNIPAM@NdFeB composites were fabricated by two-step photopolymerization. A total of 0.2 g NdFeB particles were added into 2 mL prepolymer solution of 0.2 g NIPAM, 8 mg NMBA, and 50 µL initiator (DEAP/DMF = 10 v/v%), which was then sonicated for 20 min to obtain homogeneous solution. The prepolymer solution was rapidly injected into a homemade device of a teflon spacer (3.0 cm × 0.1 cm, 200.0 µm thick) sandwiched by two glass slides, and subsequent UV-induced (365 nm) polymerization for 10 min at room temperature. Afterwards, the residual solution was removed and the teflon spacer was changed into a larger size (3.0 cm × 1.0 cm, 200.0 µm thick). Two milliliter prepolymer solution containing 0.2 g NIPAM, 8 mg NMBA, and 50 µL initiator (DEAP/DMF = 10 v/v%) was rapidly injected into the spacer, and then covered with another glass slide for UV irradiation for 10 min at room temperature. The obtained hydrogel composite was washed extensively with ultra-pure water to remove the residues. Finally, hydrogel-based millirobots with NdFeB solely in the head were facilely obtained in large-quantity via cutting the hydrogel film with certain widths and lengths (174 µm thick).

For shape-adaptable millirobots, a photomask that had black stripes (1.0 mm wide, 1.0 mm apart) passing at an angle of 90° to the long axis of the mask was placed on the upper glass slide during photopolymerization processes. Additionally, 16 mM AuNRs that were sythesized according to the previous work[11] were added into the prepolymer during the second step of photopolymerization. The other procedures were the same as mentioned above. For the hydrogel-based millirobots containing rhodamine B, 200 µL 10 mM rhodamine B solution was added into the prepolymer solution, and the following steps were prepared in the same manner as mentioned above.

For color-changeable millirobots, monodispersed silica particles with a diameter of 307 nm were assembled on a clean glass substrate through a drop-casting method. Afterwards, a prepolymer solution containing 10 wt% NIPAM and 0.1 wt% NMBA, and the 0.2 wt% initiator (DEAP/DMF = 10 v/v%) was rapidly injected into the homemade device (3 cm × 9 mm, 200 µm thick), followed by UV irradiation for 15 min at room temperature. Afterward, the obtained hydrogel composite was peeled off from the substract and then soaked in a 5 v/v% HF aqueous solution for 2 h, followed by washing with extensive water. Subsquently, the hydrogel sheet with inverse opal structures was transferred to a clean glass and covered with the larger teflon spacer (3.0 cm × 1.0 cm, 200.0 µm thick). Two milliliter prepolymer solution containing 0.2 g NIPAM, 8 mg NMBA, 50 µL initiator (DEAP/DMF = 10%, V/V), and 0.2 g magnetic responsive particles was placed into an ultrasonicator bath for 20 min until homogeneous dispersion. The pre-gel solution was rapidly injected into the teflon planer spacer and then covered with another glass slide for UV irradiation for 10 min at room temperature. The obtained hydrogel composite was washed extensively with water to remove the unreacted chemicals. Finally, the obtained hydrogel sheet was cut into desirable sizes.

*Magnetization of the Soft Robotics*: The magnetization profile of the obtained soft robotics can be programmed by spreading the hydrogel films on a clean glass slide and then placing it in a large uniform magnetizing field of 700 mT, as illustrated in Figure S1, Supporting Information. After magnetization, the head of the soft robot experiences magnetic torques when placed in a uniform magnetic field with the magnitude B limited to 10 mT.

*Determination of Speed and Tracking of the Soft Robot*: The calibrated binocular vision system consisting of two cameras (Blackfly S BFS-U3-16S2M, FLIR Systems, USA) with optical axes perpendicular to each other is used to determine the real-time speed and track the robot in 3D workspace. Experiments were performed on the developed software based on the C++, and data analysis was mainly performed using MATLAB and ORIGIN.

*Characterization*: The scanning electron microscopy (SEM) images were recorded by a field-emission scanning electron microscopy (Carl Zeiss Sigma 300, Germany) to determine the morphologies of the silica colloidals and the inverse opal structures. The black-white videos of various locomotion including crawling, swinging, rolling, and helical propulsion are accomplished by two cameras (Blackfly S BFS-U3-16S2M) located on the top and the side of a self-constructed magnetic control system (Figure S1, Supporting Information). The color images and videos of the camouflaged iRobot and structural color iRobot were taken with a digital camera (Canon 7D Mark II). Reflectance spectra of the structural color iRobot were measured by an Ocean Optics HR 2000+ spectrometer. The image of the dyed iRobot was observed by an optical microscope (Nikon Ti-U, Japan). UV–vis absorption spectra of dyed iRobot before and after exposure to NIR irradiation were recorded on a Shimadzu spectrophotometer (UV 2600). All the NIR-triggered shape deformations were performed under the illumination of an 808 nm NIR laser (5 W, Nanjing Laichuang Laser Technology Co., Ltd.). The infrared thermal images were determined by an infrared thermometer (NEC


© 2020 WILEY-VCH Verlag GmbH & Co. KGaA, Weinheim

R300SR). The temperatures were monitored by a digital thermometer (Kejian, PT300).

## Supporting Information

Supporting Information is available from the Wiley Online Library or from the author.

## Acknowledgements

The authors acknowledge the financial support provided by National Key R&D Program of China (2017YFA0701303), National Natural Science Foundation of China (21404116, 51903245), the joint Research Fund between the National Natural Science Foundation of China and Shenzhen (U1713201), the National Natural Science Foundation of China for Young Scholar (61703392), the Youth Innovation Promotion Association of CAS, CAS Key Laboratory of Health Informatics, Shenzhen Institutes of Advanced Technology (2011DP173015), the Special Support Project for Outstanding Young Scholars of Guangdong Province (2015TQ01R292), Guangdong-Hong Kong Technology Cooperation Funding (2017A050506040), the Fundamental Research Program of Shenzhen (JCYJ20180507182051636, KQJSCX20180330170232019, JCYJ20170413152640731), Shenzhen Peacock Plan (KQTD20170810160424889), Shenzhen Institute of Artificial Intelligence and Robotics for Society, and SIAT Innovation Program for Excellent Young Researchers (2019023).

## Conflict of Interest

The authors declare no conflict of interest.

## Author Contributions

X.D., H.C., and T.X. contributed equally to this work. X.D. and X.W. conceived the idea and supervised the study. X.D., H.C., and T.X. conducted the experiments with assistance from C.H., Y.W., Q.Z., and Y.X. X.D. designed the experiments, analyzed the results, and wrote the manuscript. All authors contributed to the discussion and interpretation of the results.

## Keywords

camouflage, color-shifting, millirobots, reconfiguration, responsive hydrogels

Received: November 5, 2019
Revised: December 9, 2019
Published online: January 7, 2020

[1] B. Hochner, *Curr. Biol.* **2008**, *18*, R897.
[2] T. L. Williams, S. L. Senft, J. Yeo, F. J. Martín-Martínez, A. M. Kuzirian, C. A. Martin, C. W. DiBona, C.-T. Chen, S. R. Dinneen, H. T. Nguyen, C. M. Gomes, J. J. C. Rosenthal, M. D. MacManes, F. Chu, M. J. Buehler, R. T. Hanlon, L. F. Deravi, *Nat. Commun.* **2019**, *10*, 1004.
[3] S. Johnsen, *Biol. Bull.* **2001**, *201*, 301.
[4] Y. Wu, T. Si, C. Gao, M. Yang, Q. He, *J. Am. Chem. Soc.* **2018**, *140*, 11902.
[5] J. Katuri, X. Ma, M. M. Stanton, S. Sánchez, *Acc. Chem. Res.* **2017**, *50*, 2.
[6] M. Wehner, R. L. Truby, D. J. Fitzgerald, B. Mosadegh, G. M. Whitesides, J. A. Lewis, R. J. Wood, *Nature* **2016**, *536*, 451.
[7] L. Zhang, P. Naumov, X. Du, Z. Hu, J. Wang, *Adv. Mater.* **2017**, *29*, 1702231.
[8] Y. Wang, H. Cui, Q. Zhao, X. Du, *Matter* **2019**, *1*, 626.
[9] X. Du, H. Cui, Q. Zhao, J. Wang, H. Chen, Y. Wang, *Research* **2019**, *2019*, 6398296.
[10] S. Li, R. Batra, D. Brown, H.-D. Chang, N. Ranganathan, C. Hoberman, D. Rus, H. Lipson, *Nature* **2019**, *567*, 361.
[11] X. Du, H. Cui, B. Sun, J. Wang, Q. Zhao, K. Xia, T. Wu, M. S. Humayun, *Adv. Mater. Technol.* **2017**, *2*, 1700120.
[12] D. P. Singh, W. E. Uspal, M. N. Popescu, L. G. Wilson, P. Fischer, *Adv. Funct. Mater.* **2018**, *28*, 1706660.
[13] W. Wang, L. A. Castro, M. Hoyos, T. E. Mallouk, *ACS Nano* **2012**, *6*, 6122.
[14] H. Xie, M. Sun, X. Fan, Z. Lin, W. Chen, L. Wang, L. Dong, Q. He, *Sci. Rob.* **2019**, *4*, eaav8006.
[15] J. Yu, B. Wang, X. Du, Q. Wang, L. Zhang, *Nat. Commun.* **2018**, *9*, 3260.
[16] D. Fan, Z. Yin, R. Cheong, F. Q. Zhu, R. C. Cammarata, C. Chien, A. Levchenko, *Nat. Nanotechnol.* **2010**, *5*, 545.
[17] Z. Zhakypov, K. Mori, K. Hosoda, J. Paik, *Nature* **2019**, *571*, 381.
[18] Y. Wu, J. K. Yim, J. Liang, Z. Shao, M. Qi, J. Zhong, Z. Luo, X. Yan, M. Zhang, X. Wang, R. S. Fearing, R. J. Full, L. Lin, *Sci. Rob.* **2019**, *4*, eaax1594.
[19] X. Wang, X.-H. Qin, C. Hu, A. Terzopoulou, X.-Z. Chen, T.-Y. Huang, K. Maniura-Weber, S. Pané, B. J. Nelson, *Adv. Funct. Mater.* **2018**, *28*, 1804107.
[20] S. Won, S. Kim, J. E. Park, J. Jeon, J. J. Wie, *Nat. Commun.* **2019**, *10*, 4751.
[21] Y. Zhang, L. Zhang, L. Yang, C. I. Vong, K. F. Chan, W. K. K. Wu, T. N. Y. Kwong, N. W. S. Lo, M. Ip, S. H. Wong, J. J. Y. Sung, P. W. Y. Chiu, L. Zhang, *Sci. Adv.* **2019**, *5*, eaau9650.
[22] T. Maric, C. C. Mayorga-Martinez, B. Khezri, M. Z. M. Nasir, X. Chia, M. Pumera, *Adv. Funct. Mater.* **2018**, *28*, 1802762.
[23] J. Li, B. E.-F. de Ávila, W. Gao, L. Zhang, J. Wang, *Sci. Rob.* **2017**, *2*, eaam6431.
[24] X. Yan, Q. Zhou, M. Vincent, Y. Deng, J. Yu, J. Xu, T. Xu, T. Tang, L. Bian, Y.-X. J. Wang, K. Kostarelos, L. Zhang, *Sci. Rob.* **2017**, *2*, eaaq1155.
[25] B. J. Nelson, I. K. Kaliakatsos, J. J. Abbott, *Annu. Rev. Biomed. Eng.* **2010**, *12*, 55.
[26] Q. Zhao, J. Wang, H. Cui, H. Chen, Y. Wang, X. Du, *Adv. Funct. Mater.* **2018**, *28*, 1801027.
[27] J. Wang, Q. Zhao, Y. Wang, Q. Zeng, T. Wu, X. Du, *Adv. Mater. Technol.* **2019**, *4*, 1900566.
[28] Q. Zhao, J. Wang, Y. Wang, H. Cui, X. Du, *Natl. Sci. Rev.* **2019**, https://doi.org/10.1093/nsr/nwz188.
[29] Q. Zhao, H. Cui, Y. Wang, X. Du, *Small* **2019**, 1903798.
[30] R. M. Erb, J. S. Sander, R. Grisch, A. R. Studart, *Nat. Commun.* **2013**, *4*, 1712.
[31] Y. Kim, H. Yuk, R. Zhao, S. A. Chester, X. Zhao, *Nature* **2018**, *558*, 274.
[32] Y. Kim, G. A. Parada, S. Liu, X. Zhao, *Sci. Rob.* **2019**, *4*, eaax7329.
[33] S. Palagi, P. Fischer, *Nat. Rev. Mater.* **2018**, *3*, 113.
[34] W. Hu, G. Z. Lum, M. Mastrangeli, M. Sitti, *Nature* **2018**, *554*, 81.
[35] H.-W. Huang, M. S. Sakar, A. J. Petruska, S. Pané, B. J. Nelson, *Nat. Commun.* **2016**, *7*, 12263.
[36] H.-W. Huang, F. E. Uslu, P. Katsamba, E. Lauga, M. S. Sakar, B. J. Nelson, *Sci. Adv.* **2019**, *5*, eaau1532.
[37] E. Diller, M. Sitti, *Adv. Funct. Mater.* **2014**, *24*, 4397.


© 2020 WILEY-VCH Verlag GmbH & Co. KGaA, Weinheim

[38] Z. Ren, W. Hu, X. Dong, M. Sitti, *Nat. Commun.* **2019**, *10*, 2703.
[39] T. Xu, J. Zhang, M. Salehizadeh, O. Onaizah, E. Diller, *Sci. Rob.* **2019**, *4*, eaav4494.
[40] S. A. Morin, R. F. Shepherd, S. W. Kwok, A. A. Stokes, A. Nemiroski, G. M. Whitesides, *Science* **2012**, *337*, 828.
[41] H. Yuk, S. Lin, C. Ma, M. Takaffoli, N. X. Fang, X. Zhao, *Nat. Commun.* **2017**, *8*, 14230.
[42] C. Xu, G. T. Stiubianu, A. A. Gorodetsky, *Science* **2018**, *359*, 1495.
[43] J. H. Pikul, S. Li, H. Bai, R. T. Hanlon, I. Cohen, R. F. Shepherd, *Science* **2017**, *358*, 210.
[44] G.-Z. Yang, P. Fischer, B. Nelson, *Sci. Rob.* **2017**, *2*, eaap9294.
[45] G.-Z. Yang, J. Bellingham, P. E. Dupont, P. Fischer, L. Floridi, R. Full, N. Jacobstein, V. Kumar, M. McNutt, R. Merrifield, *Sci. Rob.* **2018**, *3*, eaar7650.
[46] Q. Zhao, Y. Wang, H. Cui, X. Du, *J. Mater. Chem. C* **2019**, *7*, 6493.
[47] H. Cui, Q. Zhao, Y. Wang, X. Du, *Chem. - Asian J.* **2019**, *14*, 2369.
[48] Z. Li, Y. Yin, *Matter* **2019**, *1*, 550.
[49] C. Bergeles, G.-Z. Yang, *IEEE Trans. Biomed. Eng.* **2013**, *61*, 1565.
[50] M. Cianchetti, C. Laschi, A. Menciassi, P. Dario, *Nat. Rev. Mater.* **2018**, *3*, 143.


© 2020 WILEY-VCH Verlag GmbH & Co. KGaA, Weinheim